ADVANCED ELECTRONIC MATERIALS
www.advelectronicmat.de

Achieving High Thermoelectric Performance by Introducing 3D Atomically Thin Conductive Framework in Porous $Bi_2Te_{2.7}Se_{0.3}$-Carbon Nanotube Hybrids

Shuankui Li, Rui Wang, Weiming Zhu, Mihai Chu, Zhongyuan Huang, Yanjun Zhang, Wenguang Zhao, Fusheng Liu, Jun Luo, Yinguo Xiao, and Feng Pan**

Fabricating thermoelectric (TE) materials with porous structure is an effective approach to reduce lattice thermal conductivity; however, the electrical conductivity is usually severely sacrificed. In this work, a high performance porous $Bi_2Te_{2.7}Se_{0.3}$-carbon nanotube (BTS-CNTs) thermoelectric hybrid is prepared by introducing atomically thin BTS conductive networks on the BTS-CNT interface, which simultaneously possess ultralow lattice thermal conductivity and high electrical conductivity. The 3D conductive framework built by atomically thin BTS layers on CNTs enables the creation of an intimate contact with bulk BTS and serves as a fast pathway of the electric conductivity, resulting in high electrical conductivity. Meanwhile, the phonon scattering around nanopore wall is greatly enhanced, and the lattice thermal conductivity is found to be as low as 0.19 W m^{-1} K^{-1}, which is close to the minimal lattice thermal conductivity according to Debye–Cahill model. Consequently, the porous BTS/CNTs hybrid displays a high ZT value of about 1.2, which is 65% higher than that of fully dense pristine BTS. The present work demonstrates a novel and practical approach to design and fabricate high performance porous TE materials through an unconventional sacrificial template method.

1. Introduction

Thermoelectric (TE) materials for direct converting waste heat to electricity has drawn extensive attention because the world energy consumption wasted in the form of heat is >50%.[1,2] Generally, the energy conversion efficiency of thermoelectric material is defined by the dimensionless figure of merit, $ZT = S^2\sigma T/\kappa$, where σ, S, κ, and T are the electrical conductivity, Seebeck coefficient, thermal conductivity, and temperature, respectively.[3] However, widespread application of TE technology is limited by its low energy-conversion efficiency. Recently, several efficacious strategies have been successfully established to achieve high TE performance in thermoelectric materials, such as alloying,[4–6] nanostructuring or multiphase compositing,[7,8] modulation doping, and so on.[9–12] Most of these conventional strategies are aiming at reduction of the lattice thermal conductivity (κ_{latt}) by introducing phonon scattering centers in various length scales.[13,14] It is known that introducing of nanoporous structures is an effective way to suppress the κ_{latt}, which has been confirmed by experimental results in various TE materials, such as SiGe,[15] Bi_2Te_3,[16] PbTe,[17,18] SnSe.[19] However, tremendous amount of experimental results in porous TE materials revealed that the suppression of κ_{latt} is usually accompanied by the significant degradation of the σ, so that a high ZT cannot be achieved. Therefore, to design highly porous TE material with ideal hybrid structure, which could maximize suppress κ_{latt} without deterioration of σ, is a challenging and worthwhile exploration to obtain high-performance TE materials.

Introducing nanopores in TE materials is an effective approach for reducing κ_{latt} since the phonons can be intensively scattered by pores and accompanied interfaces. However, the porosity and carrier transport properties are always strongly correlated. Simply introducing highly porous structure will inevitably sacrifice σ. As a result, the reduction of κ cannot adequately compensate the severely reduction of σ, which always results in poor TE performance. This dilemma is well reflected in **Figure 1**a, where the data are taken from refs. [20–22]. It is found that for the dense $Bi_2Te_{2.79}Se_{0.21}$ bulk sample (relative density >95%), the material quality factor $\mu(m^*/m_0)^{3/2}/k_{latt}$ is relatively high. With decreasing relative density of the samples via introducing highly porous structure, the material quality factor $\mu(m^*/m_0)^{3/2}/k_{latt}$ is sharply decreased.[20] For example,

Dr. S. Li, R. Wang, W. Zhu, M. Chu, Z. Huang, Y. Zhang, W. Zhao, Prof. Y. Xiao, Prof. F. Pan
School of Advanced Materials
Peking University Shenzhen Graduate School
Shenzhen 518055, China
E-mail: y.xiao@pkusz.edu.cn; panfeng@pkusz.edu.cn
Prof. F. Liu
College of Materials Science and Engineering
Shenzhen University and Shenzhen Key Laboratory of Special Functional Materials
Shenzhen 518060, China
Prof. J. Luo
School of Materials Science and Engineering
Shanghai University
Shanghai 200444, China
The ORCID identification number(s) for the author(s) of this article can be found under https://doi.org/10.1002/aelm.202000292.

DOI: 10.1002/aelm.202000292

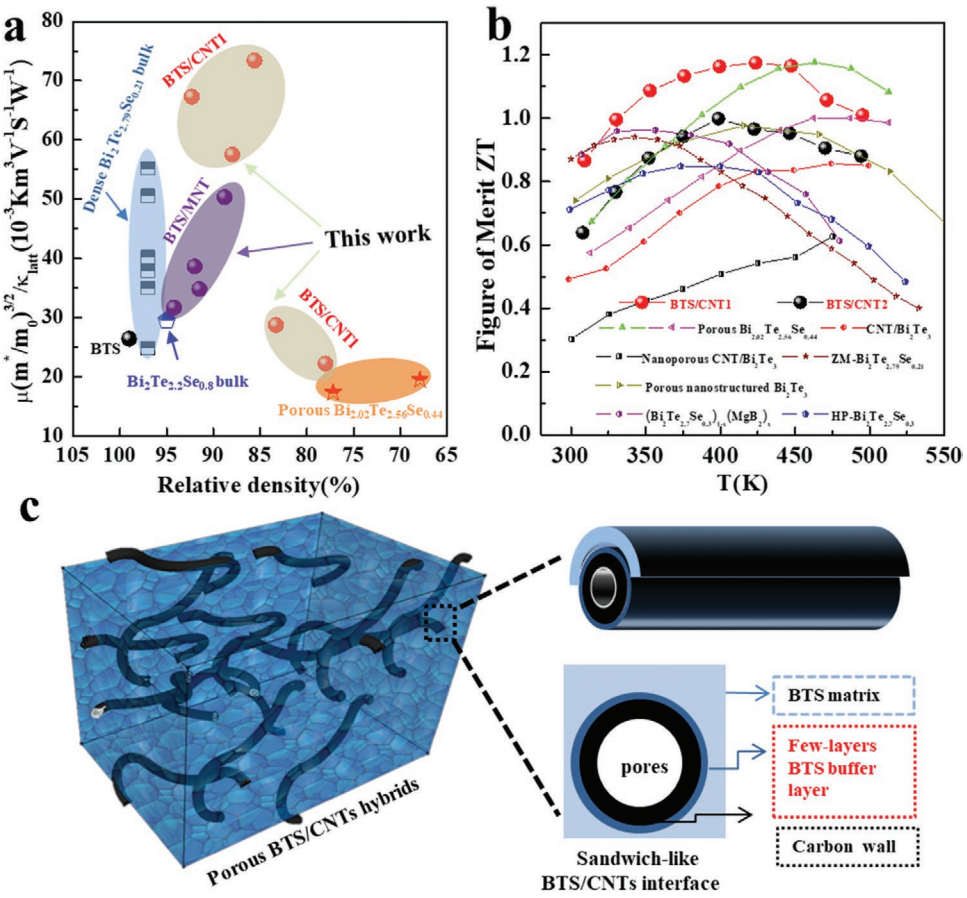

Figure 1. a) The material quality factor $\mu(m^*/m_0)^{3/2}/k_{latt}$ as a function of relative density. b) Temperature dependent zT for the as-prepared BTS/CNT samples, including a comparison to the available reference. c) sketch map of as-prepared the BTS/CNTs hybrids.

Wu et al. observed an extremely low κ_{latt} of ≈0.14 W m^{-1} K^{-1} in $Bi_2Te_{2.5}Se_{0.5}$ nanostructures with high porosity (32%). [22] However, the material quality factor $\mu(m^*/m_0)^{3/2}/k_{latt}$ is only ≈17.3 K m^3 V^{-1} S^{-1} W^{-1} due to low carrier mobility, which could be ascribed to the absence of a conduction medium in the pores as well as the pore-interface scattering of carriers.[23,24]

Therefore, functionally modifying pore interface to optimize the electrical and thermal transport behavior and introducing a hierarchical microstructure to improve the electrical connections are expected to enhance the TE performance of the porous materials.[25,26] Compared with other conventional approaches, the sacrificial template-based strategy offers a great possibility to construct idea porous TE materials. Generally, the materials with hollow structure as well as high σ, such as carbon nanotubes (CNTs) and nano onion-like fullerenes, could be used to construct nanoporous structure. However, the TE performances of the reported CNTs-based composites are still very low because of the non-uniform dispersion of CNTs and the weak interfacial interactions between matrix and CNTs.[27] While the excessive Te with low melting point could be employed to optimize the hierarchical microstructure of pore interface and improve the electrical connections between the pore wall and matrix via liquid sintering process. Moreover, by precisely controlling the hierarchical microstructure and chemical composition of pore-wall/interface, the electrical and thermal transport behavior could be further optimized, which guarantee the low κ and high σ of the as-prepared porous materials. This provides a great space and possibility to rational design and fabrication of porous materials with excellent comprehensive properties.

Here, we propose a sacrificial template-based strategy to in situ introduce the highly porous structure and construct the 3D conductive framework for high performance porous TE composites. The amorphous carbon coated Te nanowires (C@Te NWs) are used as sacrificial template, in which the Te NWs core could liquefy and penetrate into matrix-CNTs interfaces during the Spark Plasma Sintering (SPS) process and results in the formation of nanoporous structures as well as 3D conductive framework. Due to the electrical conductivity of atomically thin BTS layers formwork and good bulk BTS-pore contact, the carrier transport behavior is almost unaffected, which is almost impossible for the traditional porous thermoelectric materials. The as-prepared BTS/CNTs hybrids reveal both large material quality factor $\mu(m^*/m_0)^{3/2}/k_{latt}$ and low relative density, which is close to ideal porous thermoelectric materials. The highest power factors (PF) of the BTS/CNTs hybrids (85.6%) is as high as 22 μW cm^{-1} K^{-2}, which is comparable to that of the pristine BTS (22.8 μW cm^{-1} K^{-2}). Importantly, it is found that the

phonon scattering at the sub-nano-BTS/CNTs interface is effectively enhanced and the lowest κ_{latt} is only about 0.19 W m^{-1} K^{-1}, which is near to the calculated κ_{lmin} using Debye–Cahill model. As a result, the maximum *ZT* for BTS/CNT1–4% is 1.2 at 425 K, superior to other n-type BTS-based materials reported before (Figure 1b). The present work demonstrates a strategy to design and fabricate high performance porous TE materials through an unconventional sacrificial template method.

2. Results and Discussion

Figure 1a shows the relative density dependent material quality factor $\mu(m^*/m_0)^{3/2}/k_{latt}$ for as-prepared BTS/CNTs hybrids in this work, with literature results of dense $Bi_2Te_{2.79}Se_{0.21}$ bulk and porous $Bi_{2.02}Te_{2.56}Se_{0.44}$ for comparison.[20–22] The ideal porous thermoelectric materials possess both large material quality factor $\mu(m^*/m_0)^{3/2}/k_{latt}$ and low relative density, as shown in Figure 1a. However, it is shown that the material quality factor $\mu(m^*/m_0)^{3/2}/k_{latt}$ is sharply decreased with decreasing the relative density of the samples via introducing highly porous structure. This is due to the deterioration of σ according to recent report.[28] In present work, we employ C@Te NWs as sacrificial to in situ introduce the highly porous structure and construct the 3D conductive framework (Figure 1c), and the above problem is resolved. As shown in Figure 1a, the as-prepared BTS/CNTs hybrids reveal both large material quality factor $\mu(m^*/m_0)^{3/2}/k_{latt}$ and low relative density, which is close to ideal porous thermoelectric materials. Figure 1b compares ZT obtained in this work with reported highest ZT values for the n-BTS in literature, which indicates that the thermoelectric performance of the BTS/CNTs is substantially better than that reported in previous work, especially in the near room temperature range.[22,23,28–31]

Process of fabricating highly porous BTS/CNTs hybrids can be regarded as the C@Te NWs-based sacrificial template strategy as shown in **Figure 2**. Specifically, the C@Te NWs are synthesized first via a facile two-step solvothermal route as

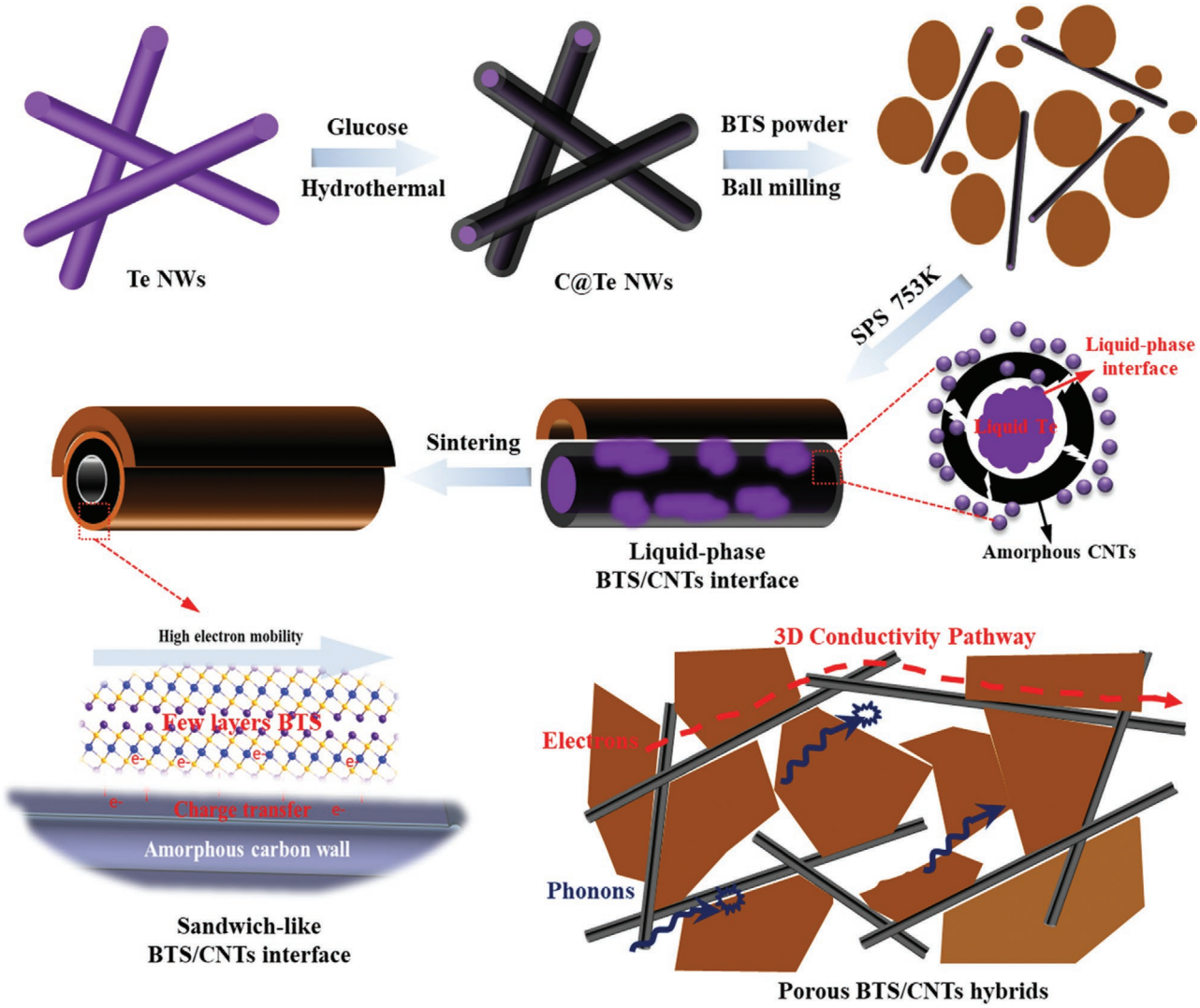

Figure 2. Fabrication process and formation mechanism of BTS/CNT porous hybrid bulk.

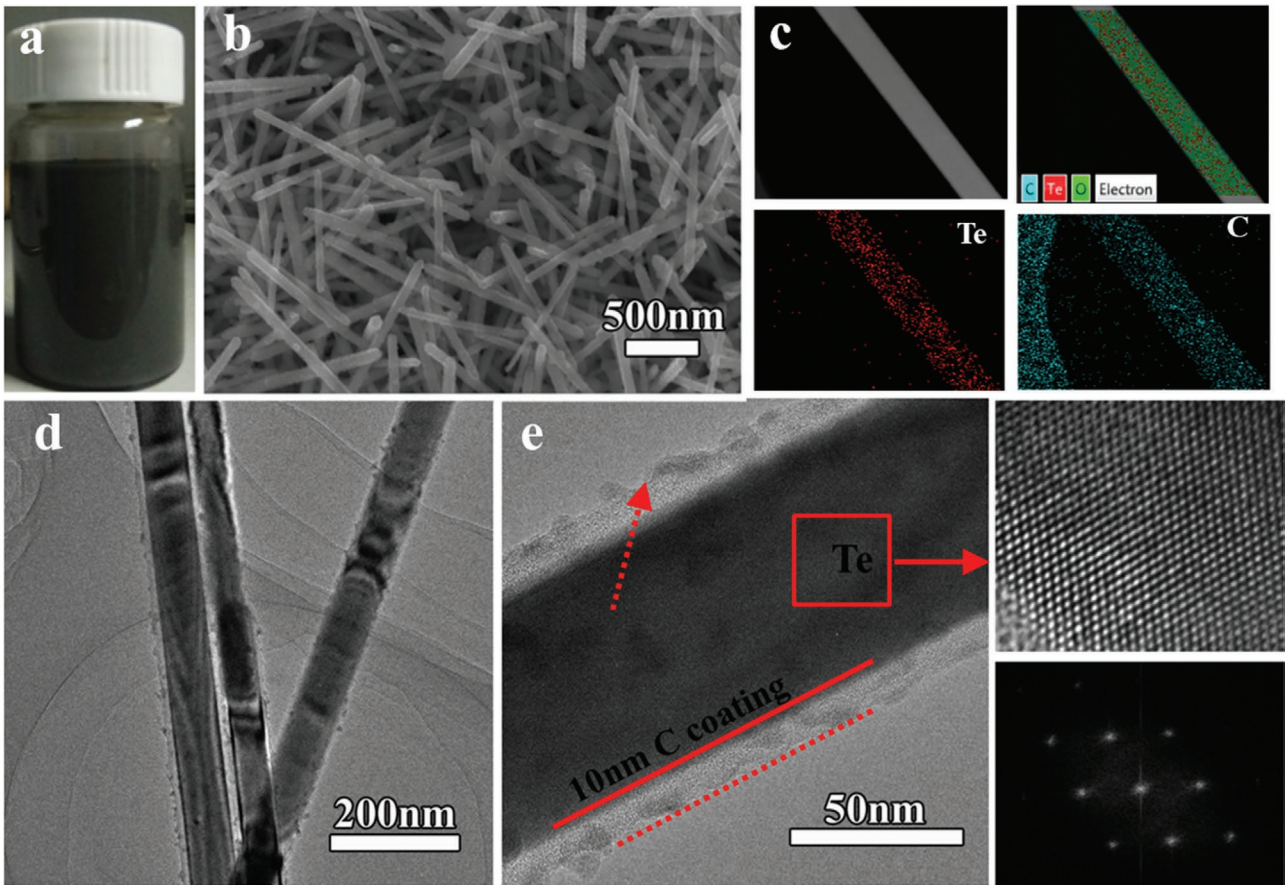

Figure 3. The morphology of the as-prepared C@Te nanowires. a) The C@Te nanowires dispersed in ethanol. b) FE-SEM image and c) the corresponding EDS pattern of the C@Te nanowires. d) TEM and e) HRTEM images.

previously reported.[32,33] The preparation of C@Te NWs started with the synthesis of Te NWs as the template, followed by a carbon coating process to obtain the C@Te NWs. The high dispersity of C@Te NWs is propitious to uniformly distribute the final CNTs in the matrix material (**Figure 3**a), which has great advantages over the hard-separated conventional CNTs. The as-prepared Te NWs are about 60–100 nm in diameter and dozens of micrometers in length (Figure 3b), and its purity is confirmed by XRD (Figure S1, Supporting Information). Importantly, the diameter of the Te NWs can be controlled by adjusting the PVP content during the hydrothermal process. As shown in Figure S2, the ultrathin Te NWs with a about 10-20 nm diameter is synthesized. A simple hydrothermal carbonization process using glucose as carbon source is employed to coat a carbon shell of about 10 nm onto the Te NWs. It is noted that the carbon shell shows a porous nature, which conformed by the TEM as well as the previous reported (Figure 3c–e). [34] During the SPS process under a high pressure and high temperature, the melting Te will penetrate into the surface of porous CNTs, which results in the reconstruction of BTS/CNTs interface by local liquid phase process. It is noted that the as-prepared C@Te NWs have an excellent dispersibility in alcohol, which ensures the uniform distribution of nanopores in bulk sample without any agglomeration. The highly porous BTS/CNTs bulk pellets are fabricated by SPS. During the SPS process under a high pressure (60 MPa) and high temperature (753 K, above the melting point of Te) environments, the Te NWs core should liquefy and penetrate into BTS/CNTs interface, which may lead to the formation of sub-nano-BTS/CNTs interface. On the other hand, the amorphous carbon shell could further carbonize, and maintain nanopore structures in the BTS matrix.

The detailed microstructure of the porous BTS/CNTs bulk materials with well-distributed nanoholes are carried out by SEM and TEM. According to the SEM image of the fracture surface (**Figure 4**a), high-density uniform pores embedded in the BTS grains are observed, which conform with the holes produced by Te evaporation during SPS process. The low-magnification TEM images also conform that high-density nanoholes are uniformly dispersed within BTS matrix without any agglomeration (Figure 4b). It is noted that for the porous BTS/CNTs bulk sample, the nanoholes are linked together to form a 3D structure, which can be observed in TEM images as well as the cross-section SEM images of the sample cut by FIB (Figure S3, Supporting Information). Moreover, the bulk samples contain two types of nanoholes, the high-density uniform 3D nanoholes embedded in the BTS grains as well as the lager voids constructed by BTS nanocrystalline. The HRTEM image clearly reveals that an ≈10 nm amorphous carbon wall exists

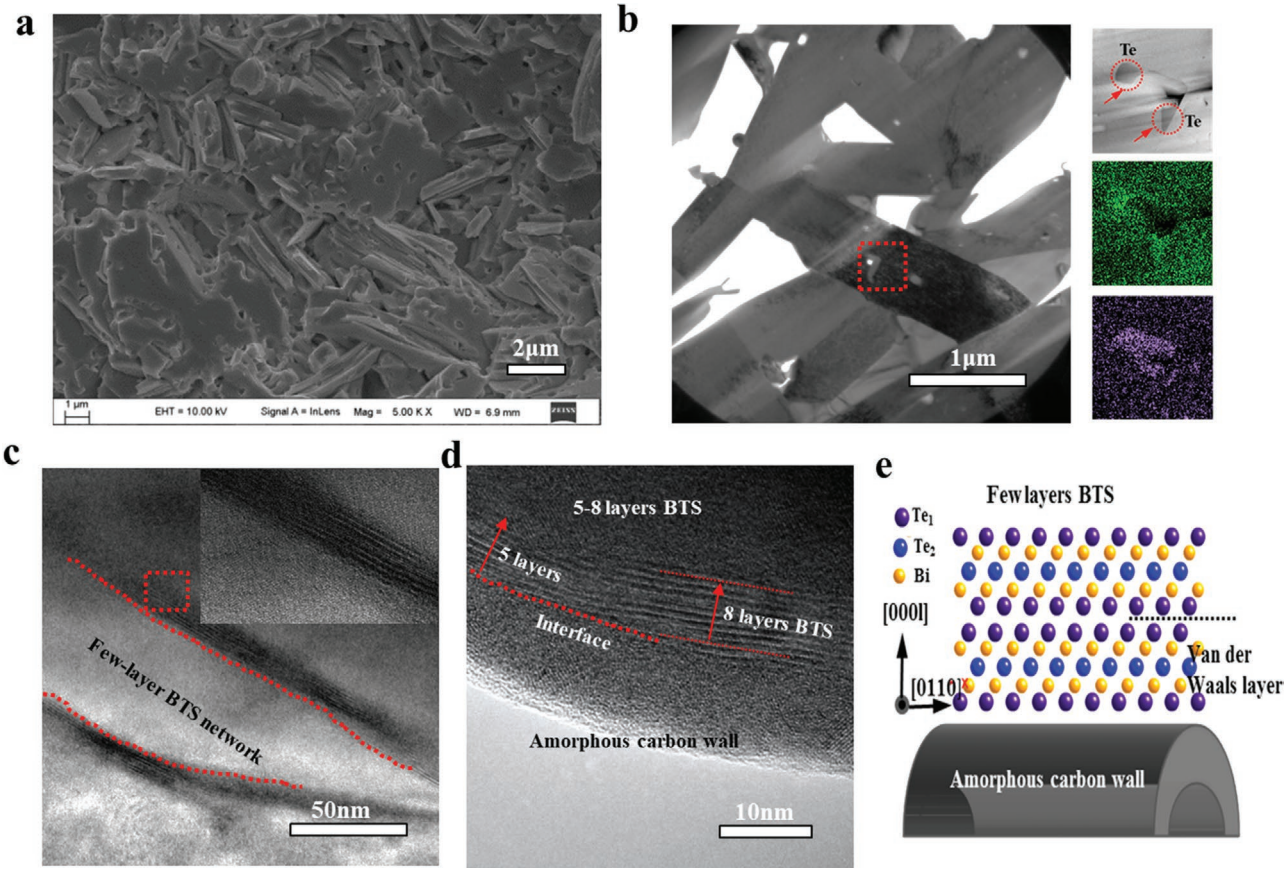

Figure 4. The microstructure of the porous BTS/CNT1 hybrid. a) FE-SEM images of the fractured surfaces of BTS/CNT1 hybrid. b) TEM image and corresponding EDS mapping images. c,d) HRTEM images of the BTS/CNT interface. e) A sketch map of the BTS/CNT interface.

at the edge of nanoholes and some small Te regions embed in the amorphous carbon wall (Figure 4d). All of these results prove that the nanoholes are mainly resulted from the evaporation and exudation of Te NW cores under SPS process. Importantly, a sub-nano-layer containing five to eight BTS quintuple layers along *c*-axis is observed between the amorphous carbon wall and BTS matrix (Figure 4b,d). Interestingly, the *c*-axis of the sub-nano-BTS layer is almost perfectly perpendicular to the surface of amorphous carbon wall (Figure 4e), even when it is highly curved, which originate from the reconstruction of BTS/CNTs interface under liquid phase process. During SPS process under a high pressure and high temperature, the Te NW cores (melting point: ≈455 °C) melt and penetrate into the surface of porous CNTs, which dissolve some of the BTS near the porous CNTs surface. When the temperature decreases, the dissolved BTS heterogeneously nucleates and grows along *c*-axis on the surfaces of the porous CNTs due to its anisotropic crystal structure. This in situ growth of the sub-nano-BTS layers ensures that it exists on almost all of the nanoholes surface (Figure S3c,d, Supporting Information), which are linked together to form a 3D structure that enables to create a close contact with bulk BTS. With increasing C@Te NWs content, the density of nanopores and the porosity of the sample are all greatly increased, which is confirmed by the SEM images shown in Figures S4 and S5, Supporting Information.

The thermoelectric properties of as-prepared porous hybrids are measured in order to investigate the structure related carrier/phonon transport behavior. As shown in **Figure 5**, the as-prepared porous BTS/CNT1 samples exhibit high electrical transport performance and extra-low κ_{tot}, leading to extraordinarily high ZTs. For all samples, σ decreased with increasing temperature, which in agreement with the previous reports (Figure 5a). As the content of C@Te NWs rises, the relative density of the sample gradually decreases from 99% (BTS) to 83.3% (BTS/CNT1-5%), while the σ only decreases slightly. Moreover, the absolute value of S for the BTS/CNT1 increases slightly, particularly for the samples with low relative density (BTS/CNT1–4% and BTS/CNT1–5%; Figure 5b). The power factors ($PF=S^2\sigma$) of the BTS/CNT1–4% with a low relative density (85.6%) is as high as 22 μW cm^{-1} K^{-2}, which is comparable to that of the pristine BTS (22.8 μW cm^{-1} K^{-2}; Figure 5c). Obviously, unlike previous studies about the thermoelectric materials with porous microstructure, the carrier transport properties of as-prepared highly porous BTS/CNT1 hybrids do not deteriorate significantly, which may be ascribed to the unique structure of BTS/CNTs interface as-maitioned above. Interestingly, all the BTS/CNT1 samples have much lower κ_{tot} than that of pristine BTS, reaching the minimum value of 0.72 W m^{-1} K^{-1} for BTS/CNT1–5%, about 44% reduction as compared with fully dense BTS matrix (1.29 W m^{-1} K^{-1}; Figure 5d). This significantly reduced

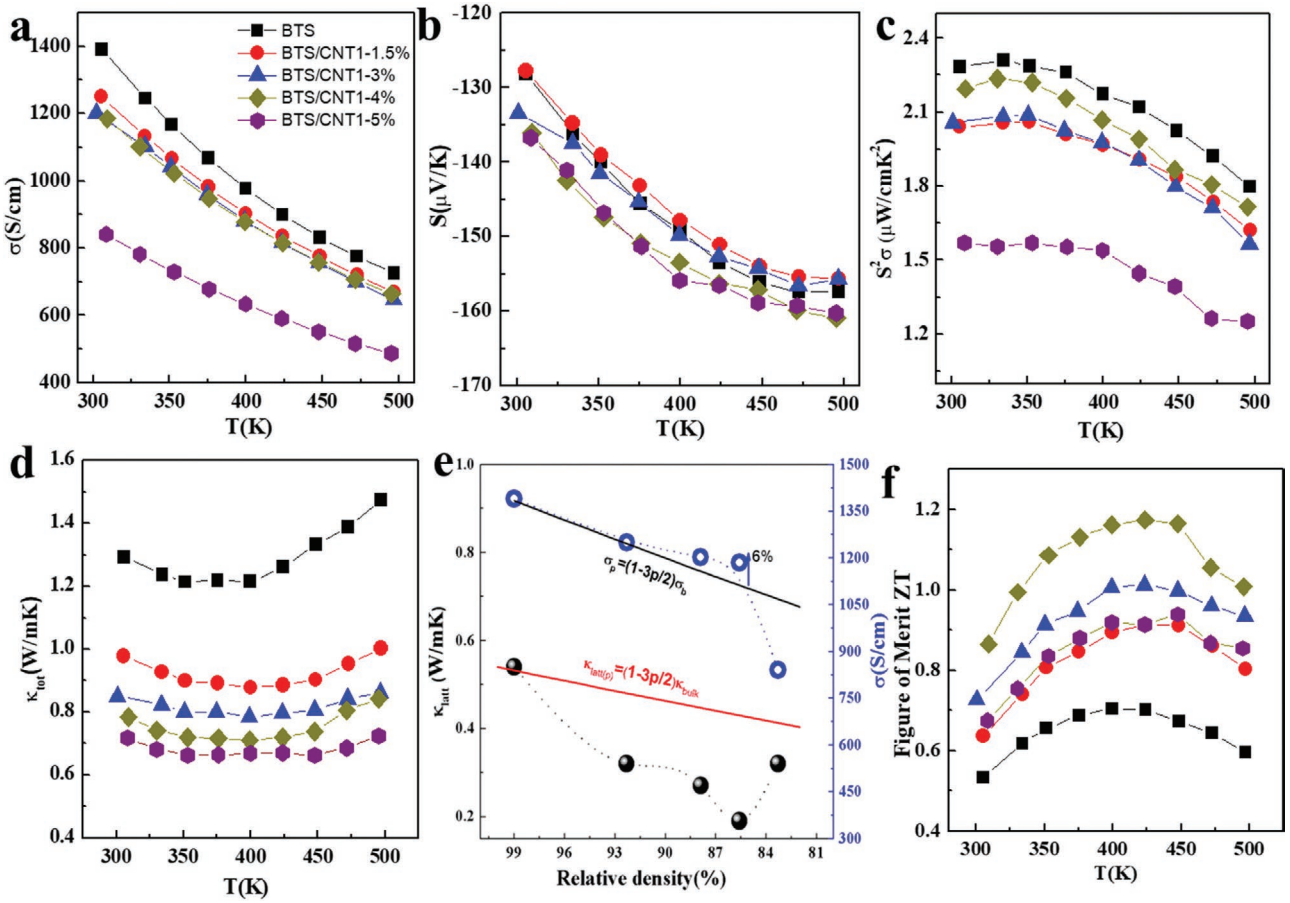

Figure 5. Thermoelectric transport properties of the porous BTS/CNT1 hybrids. a) Electrical conductivity (σ), b) Seebeck coefficient (S), c) power factor ($S^2\sigma$), and d) total thermal conductivity(κ_{tot}). e) Electrical conductivity and lattice thermal conductivity dependence of relative density of the porous BTS/CNT1 hybrids at 300 K. b) Hall carrier concentration dependence of Hall mobility at 300 K. f) Thermoelectric figure of merit ZT.

κ_{tot} is mainly ascribed to the extremely low κ_{latt}, which is near the minimum value of amorphous Bi_2Te_3 (Figure 5e).[25,35] Based on the measured electrical and thermal transport properties, the BTS/CNT1 hybrid materials possess greatly improved ZTs with a maximum value of 1.2 at 425K for BTS/CNT1-4%, which is about 65% higher than that of the pristine BTS (Figure 5f).

To describe the effects of nanopores on the electrical and thermal transport behavior, a classical effective medium theory (EMT) model is employed, which is often used to describe the simple hollow structure defined as a solid structure with a void space.[36] For a porous material with a porosity p, the electrical conductivity would be $\sigma_p = \sigma_d\, f_\sigma(p)$ and the lattice thermal conductivity would be $\kappa_{lp} = \kappa_{ld}\, f_\kappa(p)$, where f is EMT function, σ_p/κ_{lp} and σ_d/κ_{ld} present the electrical conductivity/lattice thermal conductivity of porous and dense materials, respectively.[25,37,38] The EMT function is given as follows:

$$f_k(p) = \frac{1-\varphi_n}{1+\Lambda_b\left[\dfrac{3\alpha_n\varphi_n}{2(\alpha_n+2)*d_n}\right]} \qquad \Lambda_b = \frac{3\kappa_{lb}}{C_\upsilon \upsilon_a}$$

$$\varphi_n = \frac{1}{6}\pi C_n d_n^3\left[\frac{(\alpha_n+1)(\alpha_n+2)}{\alpha_n^2}\right]$$

where α_n, d_n, and C_n are the "shape" parameter of the gamma distribution, the average diameter of nanopores, and the number density of nanopores, respectively.[19,39] Λ_b is the phonon mean free path, C_υ is the volume heat capacity, and υ_a is the average sound velocity. It is found that EMT function depends weakly on the shape of the pores to first order $f_\sigma(p) = f_\kappa(p) = (1 - 3p/2)$ and the Hall mobility and carrier concentration decrease by $(1 - 3p/4)$.[25] To study the impact of nanopores, the σ and κ_{latt} at 300 K of the as-prepared BTS/CNT1 samples were plotted versus the relative density, as shown in Figure 5e. Note that compared with the curve calculated by the EMT model, the as-prepared BTS/CNT1 samples have slightly higher σ values (except BTS/CNT1–5%) due to the high carrier concentration (Table S1, Supporting Information). The carrier concentration gradually increases from 4.7×10^{19} cm^{-3} (pristine BTS) to 5.25×10^{19} cm^{-3} (BTS/CNT1–4%), while the carrier mobility only decreases from 184.8 $cm^2\ V^{-1}\ S^{-1}$ (pristine BTS) to 141.1 $cm^2\ V^{-1}\ S^{-1}$ (BTS/CNT1–4%). Compared with the values calculated EMT model, the results are unusual, which could be ascribed to the unique structure containing 3D conductive network of the as-prepared BTS/CNT1 samples.[19,39] Note that for the BTS/CNT1–5%, the σ is distinctly lower than that calculated by the EMT model due to low carrier mobility, which is mainly attributed to the formation of lager pores in the bulk sample

due to aggregation of C@Te NWs (Figure S6, Supporting Information). It is interesting that the κ_{latt} of the BTS/CNT1 is dramatically affected, which is lower than the results calculated by the EMT model. For pristine BTS, the κ_{latt} is ≈0.54 W m^{-1} K^{-1} at 300 K, consistent with the reported results for fully densified sample.[40] But it is only ≈0.19 W m^{-1} K^{-1} for BTS/CNT1–4% (relative density is 85.6%), which shows 55% reduction as compared with the value calculated by the EMT model. This value is even lower than the calculated κ_{lmin} using Debye–Cahill model.[40] By applying the phonon gas theory, the lattice thermal conductivity in a 3D isotropic system can be written as $\kappa_{latt} = 1/3C_V\nu l$, where C_V, ν, and l stands for the constant volume heat capacity, sound velocity, and phonon mean free path, respectively. In porous material, the C_V, v, and l should be lower than that of dense materials, because all of them should lie between that of matrix material and vacuum/gas. Thus, a large porosity leads to a much reduced C_v, ν, and l simultaneously, which result in the κ_{latt} of as-prepared BTS/CNT1 samples lower than the calculated κ_{lmin} using Debye-Cahill model for fully densified sample. Obviously, the lager deviations between the measured value and EMT model are mainly attributed to the nanoholes structure containing 3D conductive network, which is distinctly different from the simple material/air or material/vacuum interface used in EMT model.

The results shown above indicate that the unique nanoholes structure is critical to the phonon and electron transport properties of samples, which contains a 3D conductive network constructed by sub-nano-BTS layers. In this case, conductive network could reasonably endow the highly porous BTS/CNT1 samples with high σ. Moreover, the carrier concentration is unexpectedly increased for the BTS/CNT1 hybrids, suggesting the donor-like effect of the introduced amorphous carbon wall. Especially, the intimate interaction of amorphous carbon wall with BTS, in which amorphous carbon walls are parallel with the (000l)-textured orientation of the sub-nano-BTS layers, leads to more contact area and thereby promote the charge transfer.[41] As mentioned above, the larger reduction of thermal conductivity cannot be explained by the porosity alone and requires additional scattering mechanisms such as sub-nano-BTS/CNTs hybrid interface scattering. Considering the unique structure at BTS/CNTs hybrid interface, the phonon-pore scattering could be effectively enhanced, since the effective phonon scattering interface is about three times larger than the ordinary porous materials. Moreover, the phase boundary, sub-nano-BTS layer (≈5 nm), amorphous carbon wall (≈10 nm), and nanopore (60~100 nm) work together to scatter phonons with different frequencies, which is different from that the large size pore only targeted low frequency phonons as reported in many porous thermoelectric materials.[25,39] The large reduction of the thermal conductivity due to the sub-nano-BTS/CNTs hybrid interface and nanopores, along with the good electrical performance can promote the thermoelectric performance.

Considering that the BTS/CNTs hybrid interface is critical to the unusual phonon and electron transport properties, it is interesting to regulate the microstructure of the BTS/CNTs hybrids. One simple way is using ultrathin C@Te nanowires (20 nm) as sacrificial template to fabricate the BTS/CNTs hybrid sample. As show in Figure S2, Supporting Information, the ultrathin C@Te nanowires with an ≈10 nm diameter and 5 nm carbon shell is synthesized, which is used to construct the porous hybrids noted as BTS/CNT2. It is clear that the morphology of the BTS/CNT2 is significantly different from the BTS/CNT1, as shown in **Figure 6**. Clearly, for the sample BTS/CNT2, the CNT network is intimately embedded in the BTS grain boundaries, which is different from BTS/CNT1 that the CNTs are homogeneously embedded in the BTS grains (Figure 6a–c; Figure S7, Supporting Information). Importantly, similar to the reported Bi_2Te_3/CNT_S composite, the nanopores in the sample BTS/CNT2 mainly distribute on the grain boundaries and the BTS/CNT interface is clean without any buffer layers, as shown in Figure 6c. Interesting, the relative density of BTS/CNT2 first decreases (78% for BTS/CNT2–1.5%), and then increases (90.3% for BTS/CNT2–4%) with the increased content of ultrathin C@Te nanowires sacrificial template (Figure 6d). Considering that the small diameter of as-prepared ultrathin C@Te nanowires, the penetration of liquefied Te from core to the surface could be difficult during SPS process due to low Te volume fraction. Thus, larger pores as well as rough BTS/CNTs interfaces could be formed due to the weak interfacial interactions between matrix and CNTs, which is similar to the conventional CNT/Bi_2Te_3 composites. As shown in Figures S8 and S9, Supporting Information, a large number of lager pores could be observed in the SEM images of the samples (BTS/CNT2–1.5% and BTS/CNT2–3%) with low content of ultrathin C@Te nanowires sacrificial template, which is consistent with their low relative density. Note that for the BTS/CNT2 samples with high sacrificial template content (BTS/CNT2–4% and BTS/CNT2–5%), the relative density reaches 90.3% (Figure S8, Supporting Information), which could be ascribed to the above-mentioned liquid phase sintering process. The sufficient liquefied Te at the BTS/CNTs interfaces could improve the weak interfacial interactions between BTS and CNTs, which result in the high relative density of the BTS/CNT2 samples with high sacrificial template content (BTS/CNT2–4% and BTS/CNT2–5%). The thermoelectric properties of the BTS/CNT2 samples are measured to investigate the structure-related carrier/phonon transport behavior (Figure S10, Supporting Information). For all the BTS/CNT2 samples, the σ values are much lower than that calculated by the EMT model due to the low carrier mobility (Figure 6e). For instance, the carrier concentration of the BTS/CNT2–4% (5.58 cm^{-3}) is similar to that of BTS/CNT1–4% (5.28 cm^{-3}), while the carrier mobility (86.1 cm^2 V^{-1} S^{-1}) is only ≈61%. The results confirmed that the 3D conductive network constructed by sub-nano-BTS layers is essential for the high σ of BTS/CNT1. Moreover, the κ_{latt} values of the BTS/CNT2 samples agree well with the values calculated by EMT model (except BTS/CNT2–1.5% with a large amount of lager pores), which means κ_{latt} of BTS/CNT2 is dominated by the phonon scattering on the induced nanopores (Figure 6e). Based on the measured electrical and thermal transport properties, the highest ZT of 1.01 at 425 K for BTS/CNT2–5% is obtained, which reveals a 40% enhancement compared with BTS matrix (Figure 6f). The above results confirmed the microstructure and nanoholes interface structure are critical to the phonon and electron transport properties.

For the Bi_2Te_3-based alloys, the |S| and n at 300 K could be used to calculate the density-of-states effective mass (m^*), which depends on the interface potential barriers.[41,42] The m_d^*

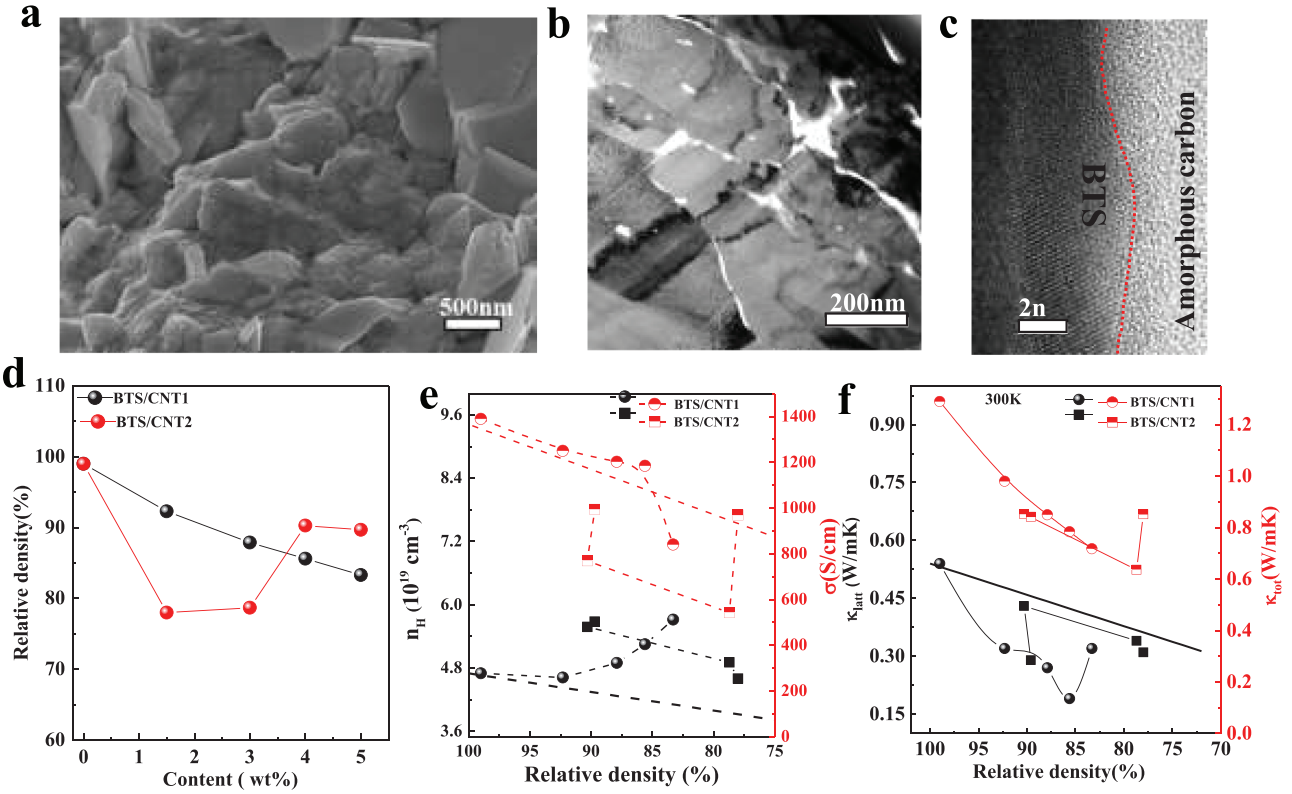

Figure 6. Morphology and thermoelectric transport properties of the porous BTS/CNT2 hybrids. a) FE-SEM images of the fractured surfaces of BTS/CNT2 hybrid. b) TEM image and c) HRTEM images of the BTS/CNT interface. d) The relative density of the BTS/CNT1 and BTS/CNT2 hybrids with different C@Te nanowires sacrificial template content. e) Electrical conductivity and carrier concentration dependence of relative density of the porous BTS/CNT1 and BTS/CNT2 hybrids at 300 K. f) Total and lattice thermal conductivity dependence of relative density of the porous BTS/CNT1 and BTS/CNT2 hybrids at 300 K.

value of BTS (≈$0.8m_0$) is almost the same to the previously reported n-type BTS-based materials.[7,8,42] For the porous samples BTS/CNT1 and BTS/CNT2, the calculated values of m^* are comparable at 300 K and indicating that the introduced porous structure may not change the band structure of the hybrids. To enhance TE performance, an increased material quality factor $\mu(m_d^*/m_0)^{3/2}/\kappa_{latt}$ is required, which could be used to determine the net gain in TE performance.[25,43] The BTS/CNT1 shows a high $\mu(m_d^*/m_0)^{3/2}/\kappa_{latt}$ value of about 57.5×10^{-3} K m^3 V^{-1} S^{-1} W^{-1}, which is far higher than that of BTS/CNT2 and the reported porous BTS thermoelectric materials. Thus, the results reveal that the high electrical conductivity and ultralow lattice thermal conductivity could be simultaneously achieved for the highly porous BTS sample by rational design the chemical composition and microstructure of the nanoholes interface, which is crucial to extend this strategy to other TE material system.

3. Conclusion

In this study, we developed a strategy to fabricate high-performance porous thermoelectric materials, using a multifunctional C@Te NWs as sacrificial template to in situ form the highly porous structure and modify the BTS/CNTs interface. The liquefying and penetration of the Te NW during the SPS process result in the sub-nano-BTS/CNTs hybrid interface, which serves as a 3D conductive network to improve the electrical conductivity of highly porous BTS/CNTs hybrids. Due to the unique structure, the high PF and ultralow lattice thermal conductivity were obtained simultaneously for the highly porous BTS/CNTs hybrids with a high porosity of ≈15%, which is contrary with the classical effective medium theory (EMT) model. An improved ZT of 1.2 is obtained, which is much higher than that of fully dense pristine BTS as well as reported n-type Bi_2Te_3-based ingot. Furthermore, by adjusting the diameter and chemical composition of sacrificial template, the microstructure, nanopore structure, and chemical composition of the porous hybrids could be controlled to investigate the structure-related phonon and electron transport behaviors. The sacrificial template-based strategy can be potentially applied to prepare other thermoelectric materials with highly porous nanostructure to optimize the thermoelectric performance.

4. Experimental Section

Synthesis of BTS Matrix: High-purity Bi, Te, and Se powders were weighed according to the stoichiometric composition $Bi_2Te_{2.7}Se_{0.3}$ and loaded into a vacuum sealed quartz tube with the diameter of 15 mm. The silica tubes were heated up to 1073 K in 5 h, soaked at this

temperature for 10 h, and subsequently cooled to room temperature in air. The obtained ingot was ground into fine powders by high energy ball-milling for 1 h.

Synthesis of Te Nanowires: TeO_2 powder (99.999%), NaOH (99.999%), thiourea, polyvinylpyrrolidone (PVP, average MW 40 000), ethylene glycol, acetone, and ethanol were purchased from the Shanghai Reagent Company. All the chemicals were used as obtained without further purification. Te nanowires were first synthesized through a simple solvothermal-based synthetic strategy. In a typical experiment, 0.96 g TeO_2, 1.2 g NaOH, and 0.4 g PVP were dissolved in 40 mL of ethylene glycol by continous stirring until all of them were dissolved. The 2 mL hydrazine hydrate solution ($N_2H_4{\cdot}H_2O$, 80%) was added to the clear solution. Then the solution was transferred into a Teflon-lined stainless autoclave (50 mL capacity), followed by solvothermal treatment at 180 °C for 18 h. The products were collected by filtration, successively washed several times with deionized water and absolute ethanol, and dried at 60 °C for 24 h.

Synthesis of C@Te Nanowires: For the synthesis of C@Te nanowires, 0.5 g of the as-prepared Te nanowires was dispersed in 40 mL of deionized water by sonication at a low-power sonic bath for 2 h. After that, 2 g glucose was added to the solution under magnetic stirring. Then the solution was transferred into a Teflon-lined stainless autoclave (50 mL capacity), followed by solvothermal treatment at 180 °C for 18 h. The products were collected by filtration, successively washed several times with deionized water and absolute ethanol, and dried at 60 °C for 24 h.

The as-prepared nanowires were first dispersed in 20 mL ethanol. After sonication at a low-power sonic bath for 2 h, the resulting solution was put together with the BTS powder and mechanical milled by using a high energy ball mill for 1 h. The products were collected by filtration, successively washed several times with deionized water and absolute ethanol, and dried at 60 °C for 24 h. Then, the products were sintered by SPS at around 753 K for 5 min under a pressure of 65 MPa.

Characterization: X-ray diffraction (XRD) was performed on a Bruker D8 Advance powder X-ray diffractometer; field-emission scanning electron microscopy (SEM) on a Zeiss SUPRA-55; and transmission electron microscopy (TEM) on a JEOL-3200F instrument.

Thermoelectric Measurements: The products were sintered by SPS at ≈753 K for 5 min under a pressure of 65 MPa. The pellets were cylinders with 10 mm in diameter and 14 mm in height. In order to avoid the anisotropic effect of the sample, the electrical and thermal transport properties were both measured along the same direction (parallel to the pressing direction of the SPS sintering). The disk with thickness of ≈2 mm was cut from the sintered pellets to measure the thermal conductivity, and a cuboid about 3 mm × 3 mm × 12 mm was cut to measure the σ and S. The electrical conductivity and Seebeck coefficient were measured using ULVAC ZEM-3 within the temperature range 300–480 K. The total thermal conductivity (κ_{tot}) was calculated through $\kappa_{tot} = DC_p\rho$, where D, C_p, and ρ are the thermal diffusivity coefficient, specific heat capacity, and density, respectively. The thermal diffusivity coefficient was measured by a laser flash apparatus using Netzsch LFA 457 from 300 to 480 K, and the specific heat (C_p) was tested by a differential scanning calorimeter (Mettler DSC1), and the density (ρ) was calculated by using the mass and dimensions of the pellet.

Supporting Information

Supporting Information is available from the Wiley Online Library or from the author.

Acknowledgements

The work was financially supported by National Materials Genome Project (2016YFB0700600), the National Natural Science Foundation of China (No. 21905007), and Shenzhen Science and Technology Research grant (No. JCYJ20150629144612861, JCYJ20150827155136104).

Conflict of Interest

The authors declare no conflict of interest.

Keywords

Bi_2Te_3, hybrids, phonon scattering, porous structures, thermoelectric materials

Received: March 20, 2020
Revised: May 1, 2020
Published online: July 14, 2020

[1] H. Zhu, C. Xiao, Y. Xie, *Adv. Mater.* **2018**, *30*, 1802000.
[2] G. J. Snyder, E. S. Toberer, *Nat. Mater.* **2008**, *7*, 105.
[3] L. E. Bell, *Science* **2008**, *321*, 1457.
[4] M. Beekman, D. T. Morelli, G. S. Nolas, *Nat. Mater.* **2015**, *14*, 1182.
[5] Y. Sadia, Z. Aminov, D. Mogilyansky, Y. Gelbstein, *Intermetallics* **2016**, *68*, 71.
[6] O. Appel, Y. Gelbstein, *J. Electron. Mater.* **2014**, *43*, 1976.
[7] S. Li, Y. Liu, F. Liu, D. He, J. He, J. Luo, Y. Xiao, F. Pan, *Nano Energy* **2018**, *49*, 257.
[8] S. Li, X. Liu, Y. Liu, F. Liu, J. Luo, F. Pan, *Nano Energy* **2017**, *39*, 297.
[9] Z. Zhou, J. Yang, Q. Jiang, J. Xin, S. Li, X. Wang, X. Lin, R. Chen, A. Basit, Q. Chen, *Chem. Mater.* **2019**, *31*, 3491.
[10] I. Cohen, M. Kaller, G. Komisarchik, D. Fuks, Y. Gelbstein, *J. Mater. Chem. C* **2015**, *3*, 9559.
[11] G. Komisarchik, D. Fuks, Y. Gelbstein, *J. Appl. Phys.* **2016**, *120*, 055104.
[12] W. Li, J. Wang, Y. Xie, J. L. Gray, J. J. Heremans, H. B. Kang, B. Poudel, S. T. Huxtable, S. Priya, *Chem. Mater.* **2019**, *31*, 862.
[13] A. Banik, T. Ghosh, R. Arora, M. Dutta, J. Pandey, S. Acharya, A. Soni, U. V. Waghmare, K. Biswas, *Energy Environ. Sci.* **2019**, *12*, 589.
[14] Y. Pan, Y. Qiu, I. Witting, L. Zhang, C. Fu, J. Li, Y. Huang, F. Sun, G. J. Snyder, C. Felser, J. F. Li, *Energy Environ. Sci.* **2019**, *12*, 624.
[15] H. Lee, D. Vashaee, D. Z. Wang, M. S. Dresselhaus, Z. F. Ren, G. Chen, *J. Appl. Phys.* **2010**, *107*, 094308.
[16] M. Takashiri, S. Tanaka, H. Hagino, K. Miyazaki, *J. Appl. Phys.* **2012**, *112*, 084315.
[17] B. Xu, T. Feng, Z. Li, S. T. Pantelides, Y. Wu, *Nano Lett.* **2018**, *18*, 4034.
[18] G. M. Guttmann, D. Dadon, Y. Gelbstein, *J. Appl. Phys.* **2015**, *118*, 065102.
[19] X. Shi, A. Wu, W. Liu, R. Moshwan, Y. Wang, Z.-G. Chen, J. Zou, *ACS Nano* **2018**, *12*, 11417.
[20] L. Hu, H. Wu, T. Zhu, C. Fu, J. He, P. Ying, X. Zhao, *Adv. Energy Mater.* **2015**, *5*, 1500411.
[21] Y. Pan, J.-F. Li, *NPG Asia Mater.* **2016**, *8*, e275.
[22] B. Xu, T. Feng, M. T. Agne, L. Zhou, X. Ruan, G. J. Snyder, Y. Wu, *Angew. Chem., Int. Ed.* **2017**, *56*, 1.
[23] Q. Zhang, L. Xu, Z. Zhou, L. Wang, W. Jiang, L. Chen, *J. Appl. Phys.* **2017**, *121*, 055104.
[24] Q. Jin, W. Shi, Y. Zhao, J. Qiao, J. Qiu, C. Sun, H. Lei, K. Tai, X. Jiang, *ACS Appl. Mater. Interfaces* **2018**, *10*, 1743.
[25] Y. Pan, U. Aydemir, J. A. Grovogui, I. T. Witting, R. Hanus, Y. Xu, J. Wu, C. Wu, F. Sun, H. Zhuang, J. Dong, J.-F. Li, V. P. Dravid, G. J. Snyder, *Adv. Mater.* **2018**, *30*, 1802016.
[26] Z. Li, J.-F. Dong, F.-H. Sun, S. Hirono, J.-F. Li, *Chem. Mater.* **2017**, *29*, 7378.
[27] R. Nunna, P. Qiu, M. Yin, H. Chen, R. Hanus, Q. Song, T. Zhang, M. Chou, M. T. Agne, J. He, G. J. Snyder, X. Shi, L. Chen, *Energy Environ. Sci.* **2017**, *10*, 1928.

[28] K. T. Kim, S. Y. Choi, E. H. Shin, K. S. Moon, H. Y. Koo, G.-G. Lee, G. H. Ha, *Carbon* **2013**, *52*, 541.
[29] Y. Wang, W. Liu, H. Gao, L.-J. Wang, M. Li, X.-L. Shi, M. Hong, H. Wang, J. Zou, Z.-G. Chen, *ACS Appl. Mater. Interfaces* **2019**, *11*, 31237.
[30] B. Chen, J. Li, M. Wu, L. Hu, F. Liu, W. Ao, Y. Li, H. Xie, C. Zhang, *ACS Appl. Mater. Interfaces* **2019**, *11*, 45746.
[31] L. Hu, H. Wu, T. Zhu, C. Fu, J. He, P. Ying, X. Zhao, *Adv. Energy Mater.* **2015**, *5*, 1500411.
[32] Z. Li, S. Zheng, Y. Zhang, R. Teng, T. Huang, C. Chen, G. Lu, *J. Mater. Chem. A* **2013**, *1*, 15046.
[33] C. Zhou, C. Dun, K. Wang, X. Zhang, Z. Shi, G. Liu, C. A. Hewitt, G. Qiao, D. L. Carroll, *Nano Energy* **2016**, *30*, 709.
[34] J. Xu, S. Xin, J.-W. Liu, J.-L. Wang, Y. Lei, S.-H. Yu, *Adv. Funct. Mater.* **2016**, *26*, 3580.
[35] Y. Zhang, T. Day, M. L. Snedaker, H. Wang, S. Krämer, C. S. Birkel, X. Ji, D. Liu, G. J. Snyder, G. D. Stucky, *Adv. Mater.* **2012**, *24*, 5065.
[36] F. Hu, S. Wu, Y. Sun, *Adv. Mater.* **2018**, *24*, 5065.
[37] H. J. Juretschke, R. Landauer, J. A. Swanson, *J. Appl. Phys.* **1956**, *277*, 838.
[38] D. J. Bergman, O. Levy, *J. Appl. Phys.* **1991**, *70*, 6821.
[39] J. K. Carson, S. J. Lovatt, D. J. Tanner, A. C. Cleland, *Int. J. Heat Mass Transfer* **2005**, *48*, 2150.
[40] K. Zhao, H. Duan, N. Raghavendra, P. Qiu, Y. Zeng, W. Zhang, J. Yang, X. Shi, L. Chen, *Adv. Mater.* **2017**, *29*, 1701148.
[41] Q. Jin, S. Jiang, Y. Zhao, D. Wang, J. Qiu, D.-M. Tang, J. Tan, D.-M. Sun, P.-X. Hou, X.-Q. Chen, K. Tai, N. Gao, C. Liu, H.-M. Cheng, X. Jiang, *Nat. Mater.* **2019**, *18*, 62.
[42] S. Li, C. Xin, X. Liu, Y. Feng, Y. Liu, J. Zheng, F. Liu, Q. Huang, Y. Qiu, J. He, J. Luo, F. Pan, *Nano Energy* **2016**, *30*, 780.
[43] B. Zhu, N. Liu, M. McDowell, Y. Jin, Y. Cui, J. Zhu, *Nano Energy* **2015**, *13*, 620.

